Appl Phys B (2009) 94: 187–194
DOI 10.1007/s00340-008-3274-1

Applied Physics B
Lasers and Optics

Modulation control and spectral shaping of optical fiber supercontinuum generation in the picosecond regime

G. Genty · J.M. Dudley · B.J. Eggleton

Received: 29 July 2008 / Revised version: 9 October 2008 / Published online: 6 November 2008

Abstract Numerical simulations are used to study how fiber supercontinuum generation seeded by picosecond pulses can be actively controlled through the use of input pulse modulation. By carrying out multiple simulations in the presence of noise, we show how tailored supercontinuum spectra with increased bandwidth and improved stability can be generated using an input envelope modulation of appropriate frequency and depth. The results are discussed in terms of the nonlinear propagation dynamics and pump depletion.

PACS 42.65.-k · 42.81.Dp

1 Introduction

Following its first observation by Ranka et al. in 1999–2000 [1], supercontinuum (SC) generation in photonic crystal fiber has remained a subject of intense research. Motivated by important applications in precision frequency metrology, initial effort focussed on developing a clear physical understanding of the underlying mechanisms and noise properties of SC generation seeded by femtosecond pump pulses, a regime which is now very well understood [2–5]. Research is now shifting towards detailed studies of the dynamical properties for cases where spectral broadening is initiated in the so-called "long-pulse" regime, using picosecond to nanosecond pulses, or even a continuous wave pump. In fact, under these conditions and pumping in the anomalous dispersion regime, the SC spectral broadening has been shown to be associated with a very rich range of dynamical behavior, involving spontaneous pulse break up due to modulation instability (MI) followed by the propagation and interaction between very large numbers of ejected soliton pulses [5–13].

Recent results have extended this research even further, identifying significant links with other areas of nonlinear physics. Particular insight into the mechanism underlying SC fluctuations in the long-pulse regime was provided by Solli et al. who used a novel real-time detection technique to directly quantify the statistics of picosecond SC shot-to-shot noise [14]. This work was significant in showing that the SC fluctuations led to the generation of "optical rogue waves," statistically rare extreme red-shifted Raman solitons on the long wavelength edge of the SC spectrum. Further numerical analysis of these fluctuations in [15] showed explicitly that the rogue soliton statistics exhibit non-Gaussian extreme-value characteristics. In fact, non-Gaussian statistics due to soliton collisions in the presence of Raman scattering had been studied earlier in the context of multichannel fiber communications systems [16–23], but possible links with the soliton dynamics of supercontinuum generation [6, 7] were not explored. Related studies of a fundamental nature in the long-pulse regime have applied results from weak turbulence theory to describe the initial spectral broadening as

G. Genty
Optics Laboratory, Department of Physics, Tampere University of Technology, 33101 Tampere, Finland
e-mail: goery.genty@tut.fi

J.M. Dudley
Institut FEMTO-ST, Département d'Optique P. M. Duffieux, CNRS UMR 6174, Université de Franche-Comté, 25030 Besançon, France
e-mail: john.dudley@univ-fcomte.fr

B.J. Eggleton
CUDOS ARC Centre of Excellence, School of Physics, University of Sydney, NSW 2006, Sydney, Australia
e-mail: egg@physics.usyd.edu.au

a "sea of solitons," and the associated semiclassical scattering problem has been shown to analytically model experimentally measured SC spectra [24].

From an applications perspective, controlling SC bandwidth and stability is very important, and indeed, guidelines for broadband and low-noise SC generation using sub-50 fs femtosecond pulses are well known [5]. Studies in the femtosecond regime have also shown how the generated SC spectra can be controlled by varying the input conditions in a more sophisticated manner, using chirped input pulses to modify the propagation dynamics [4, 25], using dual frequency femtosecond pumping to induce cascaded four wave mixing [26], or using femtosecond envelope modulation to influence the Raman soliton noise properties [27]. Additional methods of SC control around telecommunications wavelengths and techniques for noise reduction in pulse train generation have also been studied [28–30].

In the long-pulse regime, modified initial conditions can also significantly influence the output SC characteristics and stability. For example, Solli et al. numerically demonstrated a correlation between rogue soliton pulse height and a low-amplitude localized noise burst on the leading edge of the picosecond pump pulses [14]. This idea was extended in [15], where numerical simulations were again used to show that modified rogue soliton statistics could be observed using a ∼4% intensity modulation across the full extent of the pulse envelope. A recent eprint by Solli et al. has reported significant experimental results, showing that seed modulation of SC generation at the −30 dB level can also introduce an effective phase transition in the SC stability [31].

The dramatic effect of these modified input conditions illustrate the sensitivity of the initial MI propagation phase of long-pulse SC generation to coherent input modulation. However, the studies described above have considered only the effects of weak perturbations over a limited parameter range, whereas it might be expected that the induced SC dynamics will depend very sensitively on both the frequency and amplitude of any applied modulation. Our objective in this paper is therefore to examine the potential parameter space of input modulation more extensively, focussing on how both the SC spectral intensity and stability are modified as functions of the modulation parameters. A major result is the discovery that certain modulation parameters yield stabilized spectra with Raman soliton peak power statistics transformed from an "L-shaped" extreme-value distribution to a near-Gaussian distribution with significantly reduced peak power fluctuations below 5%. We also extend previous physical discussions of the SC generation mechanism in the long-pulse regime to explicitly include the role of pump depletion. These results show that considerations of pump depletion dynamics can provide useful insight into the sensitivity of the SC broadening to input pulse modulation.

2 Numerical model

Our simulations use a generalized form of the well-known nonlinear Schrödinger equation suitable for modeling propagation of broadband unidirectional fields [5, 32]. With explicit inclusion of higher-order linear and nonlinear terms, it can be written in the following way:

$$\begin{aligned}\frac{\partial A}{\partial z}+\frac{\alpha}{2}A-\sum_{k\geq 2}\frac{\mathrm{i}^{k+1}}{k!}\beta_k\frac{\partial^k A}{\partial T^k}\\ =i\gamma\left(1+i\tau_{\mathrm{shock}}\frac{\partial}{\partial T}\right)\\ \times\left(A(z,t)\left[\int_{-\infty}^{+\infty}R(T')\left|A(z,T-T')\right|^2dT'\right.\right.\\ \left.\left.+i\Gamma_{\mathrm{R}}(z,T)\right]\right).\end{aligned}\tag{1}$$

Here $A(z,t)$ is the field envelope, and the β_k's and γ are the usual dispersion and nonlinear coefficients. In our simulations we consider propagation in 25 m of fused silica based optical fiber with zero dispersion around 1055 nm. The dispersion coefficients at a pump wavelength of 1060 nm are: $\beta_2=-0.820\ \mathrm{ps}^2\,\mathrm{km}^{-1}$, $\beta_3=6.87\times10^{-2}\ \mathrm{ps}^3\,\mathrm{km}^{-1}$, $\beta_4=-9.29\times10^{-5}\ \mathrm{ps}^4\,\mathrm{km}^{-1}$, $\beta_5=2.45\times10^{-7}\ \mathrm{ps}^5\,\mathrm{km}^{-1}$, $\beta_6=-9.79\times10^{-10}\ \mathrm{ps}^6\,\mathrm{km}^{-1}$, $\beta_7=3.95\times10^{-12}\ \mathrm{ps}^7\,\mathrm{km}^{-1}$, $\beta_8=-1.12\times10^{-14}\ \mathrm{ps}^8\,\mathrm{km}^{-1}$, $\beta_9=1.90\times10^{-17}\ \mathrm{ps}^9\,\mathrm{km}^{-1}$, $\beta_{10}=-1.51\times10^{-20}\ \mathrm{ps}^{10}\,\mathrm{km}^{-1}$, and $\gamma=0.015\ \mathrm{W}^{-1}\,\mathrm{m}^{-1}$. The nonlinear response $R(t)=(1-f_{\mathrm{R}})(t)+f_{\mathrm{R}}h_{\mathrm{R}}(t)$ with $f_{\mathrm{R}}=0.18$ includes instantaneous and Raman contributions. The response h_{R} is determined from the experimental fused silica Raman cross-section [33], but similar results can be obtained using analytic approximations for the Raman term [34]. The envelope self-steepening timescale $\tau_{\mathrm{shock}}=0.658$ fs. Noise is included in the frequency domain through a one photon per mode background, and via the term Γ_{R} which describes thermally-driven spontaneous Raman scattering [5, 35]. Simulation results displayed here were obtained typically using a 50 ps time window, a minimum of 2^{15} time-frequency grid points, and 10000 longitudinal steps. To examine the SC stability characteristics, multiple simulations were carried out in the presence of different random noise seeds, allowing the spectral and temporal structure of the SC to be examined from shot-to-shot. In this regard, we have found that the spectral shape and coherence properties can be well determined using an ensemble of typically 100 realizations, although for cases where histogram data is calculated, obtaining sufficient data in the distribution tails requires larger ensembles with >1000 realizations.

We consider an input field of the form $A(0,T)=\sqrt{P_0}\exp(-t^2/2T_0^2)[1+a_0\exp(-\mathrm{i}\Omega t)]$, which corresponds

to a modulated Gaussian pulse envelope with intensity modulation contrast $2a_0/(1+a_0^2)$. A modulated envelope of this form can be generated through the beating of a pulse with a (Stokes) frequency-shifted replica, and such dual frequency fields have been previously used to generate high-repetition rate pulse trains through induced MI/four wave mixing [36–38]. We carry out simulations over a range of values of a_0 and Ω, adjusting the pump and Stokes sideband amplitude to ensure that the energy remains constant. With this approach, the individual peak powers of the pump and Stokes pulses are $P_p = P_0/(1+a_0^2)$ and $P_s = P_0 a_0^2/(1+a_0^2)$, respectively. We choose an input energy of 0.4 nJ, which corresponds to $P_p = P_0 = 75$ W at zero modulation.

3 Numerical simulations

3.1 Illustrative results

We first consider SC generation in the absence of any envelope modulation ($a_0 = 0$) seeded by pulses with $T_0 = 3$ ps and $P_0 = 75$ W. At this (anomalous dispersion) pump wavelength, the soliton order $N = (\gamma P_0 T_0^2/|\beta_2|)^{0.5} \approx 111$. Such a large value is typical for picosecond SC generation and is expected to yield significant shot-to-shot variation in both the spectral and temporal characteristics [5]. This is illustrated explicitly in Fig. 1(a), which shows results from an ensemble of 1000 simulations, plotting the output SC characteristics after 25 m propagation. Subfigures (i) and (ii) show the output spectral and temporal characteristics, respectively, superposing a subset of 75 realizations from individual simulations (gray traces) and also showing the calculated mean from the full ensemble (black line).

Figure 1 clearly shows significant shot-to-shot fluctuations in both the temporal and spectral intensities. Fluctuations in the spectral phase across the SC can be seen by plotting the spectral coherence calculated from the ensemble, and this is plotted on the right axis of subfigure (i). This coherence function corresponds to the fringe visibility at zero path difference in a Young's two-source experiment performed between independent SC spectra and is a widely used measure of SC stability [39]. Of significance here is that the shot-to-shot fluctuations essentially lead to zero spectral coherence (spectral phase stability) across the full bandwidth of the SC, except for a narrow wavelength range in the vicinity of the pump. Such instability in both the temporal and spectral properties is a well-known characteristic of SC generation using picosecond pulses, arising because spectral broadening in this regime is seeded from an ultrafast modulation that develops on the pulse envelope from noise-induced MI. As the envelope subsequently breaks up into individual soliton pulses with further propagation, the random nature of the initial modulation introduces significant shot-to-shot differences in the subsequent Raman soliton dynamics and frequency shifts.

The effect of these fluctuations on the spectral structure of the SC is illustrated in subfigure (i) of Fig. 1(a). On the long wavelength edge, we note in particular significant variation in the positions of Raman solitons, and the key result of Solli et al. was to show that these variations contain a small number of statistically-rare "rogue" events associated with a greatly enhanced red-shift [14]. Because they are rare, the rogue events do not contribute significantly to averaged spectral measurements, but they can nonetheless be individually detected through shot-to-shot analysis by positioning a spectral filter in the wings of the mean supercontinuum spectrum.

Specifically, by selecting only the components of the spectrum located beyond a certain cutoff wavelength and then Fourier transforming, we can determine the temporal profile corresponding to the filtered spectrum. Then, by analyzing an ensemble of results generated using different noise seeds, we can calculate a histogram of the peak power distribution of these profiles. In this way, femtosecond Raman solitons in the spectra that are red-shifted beyond the cutoff wavelength will be completely captured. However, because extreme red shifted solitons occur only rarely and thus form the long tail of the histogram, it is much more likely that the filtering procedure will capture only the wings of a particular supercontinuum spectrum lying close to the mean, and in this case the filtered temporal profile will yield only a non-solitonic pulse with lower peak power.

In order to apply this technique to detect rogue solitons, the filter should be placed in the wings of the mean SC spectrum. We have found from additional simulations that filter placement at a wavelength near the -3 dB rolloff of the mean spectrum effectively isolates the rogue solitons and yields the characteristic L-shaped histogram associated with extreme-value processes. For our parameters, this guideline motivates the choice of filter placement at 1180 nm. As indicated above, the solitons that are fully captured by the filtering procedure appear in the tails of the distribution, and we have been able to quantify the peak power value at which they appear by analyzing the filtered temporal profiles on a shot-by-shot basis. Specifically, by calculating the corresponding soliton number for each filtered pulse in the ensemble, we find that it is only for peak powers $\gtrsim$250 W that the filtering captures pulses that can be called "solitons" with a soliton order $N \approx 1$, and this represents only $\approx$15% of the total filtered events. Of course, the most extreme "rogue" events with peak powers exceeding 1 kW make up a much smaller fraction, occurring at the 0.1% level.

As discussed in the introduction above, the results in [15] showed how a weak envelope modulation could significantly modify these rogue soliton statistics. In this study, we have examined the effect of such input modulation for the case of higher modulation depths and have found that modulation

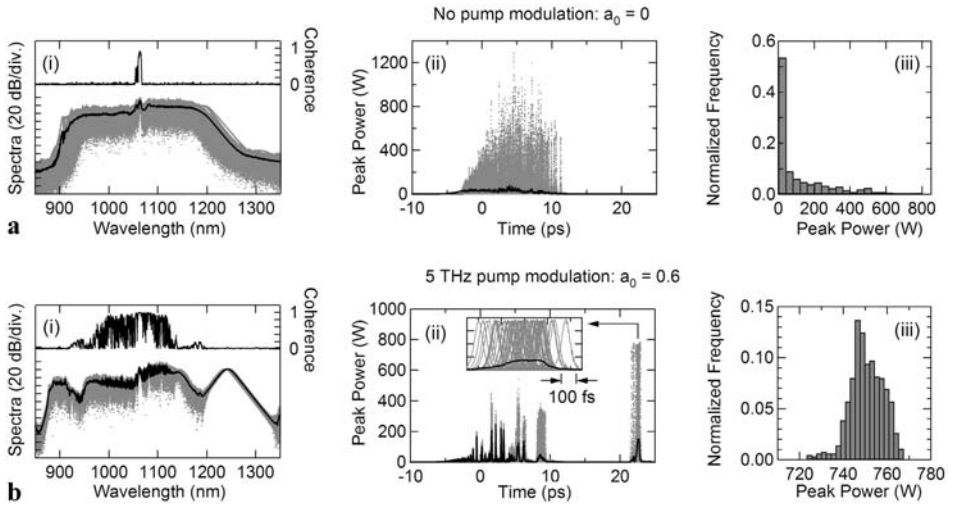

Fig. 1 Simulation results for SC induced by pulses with **a** no input modulation and **b** modulation at 5 THz and $a_0 = 0.6$. For each case, (i) and (ii) show output spectral and temporal characteristics, respectively, superposing individual simulation results (*gray traces*) with the calculated mean from the ensemble (*black line*). (i) Also plots calculated coherence on the *right axis*. (iii) Shows the peak power histogram after spectral filtering at 1180 nm, plotting normalized event frequency such that bar height represents the proportion of data in each bin. Note that coherence and statistical data are calculated from the full ensemble of 1000 realizations, but for clarity, the *gray traces* show only 75 realizations

depths above 50% in fact yield a very significant degree of control into the output SC properties compared to the case where the SC develops from noise. This is conveniently illustrated by considering a specific case, and Fig. 1(b) shows the output SC characteristics for an input field consisting of a pump at 1060 nm and a Stokes pulse of the same duration but frequency-shifted by 5 THz (i.e., at a wavelength of 1079 nm) and with $a_0 = 0.6$ such that $P_p = 55$ W and $P_s = 20$ W.

Significantly, although the peak power at the pump wavelength is reduced compared to the unmodulated case, Fig. 1(b) shows clearly that the effect of this envelope modulation leads to significantly different output characteristics for the spectral, temporal, and statistical properties. For example, subfigure (i) shows an increased overall bandwidth with extended long and short wavelength edges, improved spectral coherence, and significantly less variation in the shot-to-shot spectral structure compared to Fig. 1(a). This leads to a well-isolated Raman soliton peak on the long wavelength edge. The time domain characteristics in subfigure (ii) also show reduced shot-to-shot variation when compared to Fig. 1(a) and clearly illustrate the localized temporal structure of the Raman soliton around a time coordinate of 24 ps. However, the inset shows that although each Raman soliton has a temporal duration of ∼80 fs, the residual wavelength fluctuations result in significant temporal jitter in the soliton position of ∼1 ps. It is this temporal jitter that leads to the near zero spectral coherence in subfigure (i) in the vicinity of the Raman soliton wavelength. Nonetheless, when compared to the spontaneously generated SC in Fig. 1(a), the input modulation yields a remarkable improvement in the SC stability. This is also seen in subfigure (iii), which shows the peak power histogram after long wavelength filtering at 1180 nm. Here we see that instead of an L-shaped distribution indicative of a small number of extreme red-shifted rogue events, we obtain a significantly more localized Gaussian-like distribution. Indeed, the fluctuation in the filtered soliton pulse peak power about the mean for these parameters is only ≈5%.

3.2 Interpretation and discussion

To interpret these results physically, it is useful to consider how the SC characteristics vary over a wider range of modulation frequencies. To this end, Fig. 2 shows results for $a_0 = 0.6$ but over a 0–20 THz span of modulation frequencies. The results show (a) the mean output spectra and (b) the associated wavelength-dependent degree of coherence calculated from the ensemble. Here we plot the results using a false color representation with wavelength as the horizontal axis and modulation frequency on the vertical axis. Note that these spectral characteristics calculated over an ensemble generalize similar single-shot noise-free results used in previous work [15] and provide more realistic predictions of the spectral structure and stability properties that could be expected in experiments.

From these results we see that the output spectral structure clearly exhibits significant dependence on modulation frequency. Indeed, it can be seen that the particular frequency of the input modulation introduces a remarkable degree of control into the SC generation process, allowing both extension and reduction of the output bandwidth when compared to the unmodulated case. The dependence of the output spectral structure on modulation frequency is complex,

but useful insight can be obtained by comparing the results seen in Figs. 2(a) and (b) with the frequency-dependent gain curve describing the growth of a Stokes wave component due to MI and Raman processes. To this end, we plot in Fig. 2(c) the gain curve describing the coupling between MI and Raman gain [40], calculated for the undepleted pump wave of power P_p at the fiber input. Note that the curve is more complex than a mere superposition of the separate MI and Raman processes but nonetheless shows a clear MI gain peak around 8 THz and a distinct shoulder around the 13.2 THz peak of Raman gain in fused silica.

From inspection of Fig. 2(a) we can identify three broad ranges for the input modulation frequency that present qualitatively different output characteristics. We first consider the behavior observed for modulation frequencies less than ∼8 THz. This (approximate) upper limit corresponds to the frequency above which there is no clear evidence in Fig. 2(a) of any long wavelength spectral localization, nor is there any corresponding short wavelength dispersive wave structure far from the pump. On the other hand, for frequencies less than ∼8 THz, the output spectra extend on both the long and short wavelength side of the pump and exhibit soliton and dispersive wave structure. Of course, the most dramatic example of this structure occurs at the frequency of 5 THz, as seen in Fig. 1 above.

These characteristics illustrate the importance of soliton dynamics in this regime, arising because of the reshaping of the input pulse envelope into a train of high-contrast soliton train during the initial MI phase of propagation. Significantly, we note that the values of modulation frequency detunings where we observe these dynamics are less than the frequency of maximum MI gain. Although perhaps surprising, this can be understood from the fact that we are in a strong conversion regime, and thus the frequency of maximum MI gain dynamically shifts towards lower values with propagation as pump depletion becomes significant.

In fact, previous analytical studies of this process under CW excitation using a truncated sideband model to describe coherent pump-energy exchange have predicted maximum integrated gain with an initial modulation frequency of around half the frequency of peak MI gain calculated using the initial value of undepleted pump power [41]. Although the dynamics of the regime considered here are more complex (involving multiple sidebands and Raman scattering), such an analysis is useful for the physical interpretation of these results. In particular, we can interpret the improved coherence properties of the generated SC seen in Fig. 2(b) (see also Fig. 1(b)) as arising from the reduced influence of spontaneous MI relative to coherent exchange between the generated sidebands.

Secondly, as the modulation frequency increases into the range 8–15 THz, Fig. 2(a) now shows a predominantly red-shifted output SC spectrum where long wavelength soliton structure is no longer clearly apparent. This behavior can be readily understood from the fact that the dynamically decreasing frequency shift of the MI gain curve due to pump depletion means that increased initial modulation frequency lies outside the region of significant MI gain after a very short propagation distance, and thus the dynamics exhibit reduced coherence as reflected in Fig. 2(b). In this regime, Raman amplification plays a more significant role, and there is a predominantly red-shifted output spectrum. A more detailed analysis on a shot-to-shot basis still shows the development of red-shifted solitons from the Raman-amplified Stokes side-band, but these are not distinctly resolved in the mean spectrum.

Finally, for frequencies exceeding ∼15 THz, the input modulation lies outside the regime of significant MI and Raman gain. In this case, we see the growth of low amplitude spontaneous MI sidebands around 7 THz from the pump so that this regime is essentially similar to the incoherent and unstable case of an unmodulated pump in Fig. 1(a). A detailed consideration of this regime would, however, need to take into account energy exchange between the pump and both initial and spontaneously generated sidebands with propagation.

Figures 3 and 4 illustrate additional aspects of the dynamics for the case of an amplitude modulation $a_0 = 0.6$. Specifically, Fig. 3 highlights the importance of pump depletion in the initial phase of propagation, plotting the energy at the pump wavelength as a function of propagation distance, and for modulation frequencies over the range 1–20 THz. Note that in calculating the energy at the pump wavelength, we integrate over a 1 THz bandwidth; this is more than 10 times the initial bandwidth and allows the depletion of pump energy through gain dynamics to be fully captured while covering a bandwidth sufficient to include the broadening of the pump itself due to self-phase modulation.

The left subfigure shows results using a false color representation up to a propagation distance of 7 m, whilst the right subfigure plots the pump energy over 25 m propagation for selected modulation frequencies as shown. Although the detailed frequency and distance dependence of the pump depletion is complex, it is nonetheless clear that maximum pump depletion occurs at an earlier stage of the propagation for modulation frequencies less than 8 THz, correlating with coherent MI gain dynamics and the more distinct observed soliton features in the spectra shown in Fig. 2.

The particular modulation frequency of 5 THz considered in Fig. 1 leads to a very clear and distinct soliton component on the long wavelength edge of the output spectra, and Fig. 4 considers the corresponding time-domain dynamics in more detail. This figure shows how the evolution of the initially modulated envelope leads to the ejection of one particular high-power soliton pulse (after a distance of around 7 m) that extracts energy from the other soliton like pulses

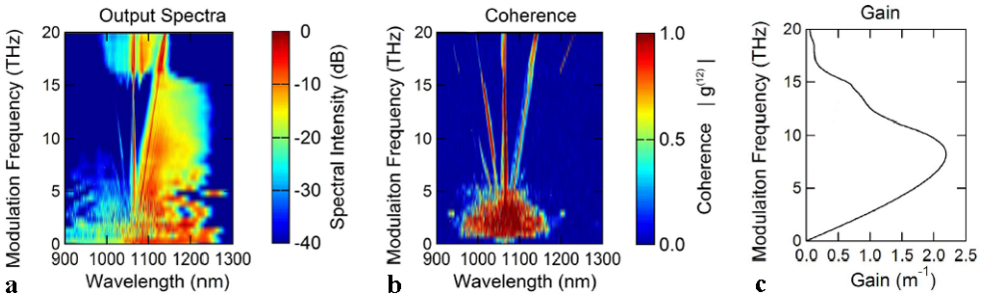

Fig. 2 **a** Density plot of output spectral intensity after 25 m propagation for $a_0 = 0.6$ as a function of applied modulation frequency (*vertical axis*). **b** Corresponding degree of spectral coherence. **c** Calculated mixed MI-Raman gain curve

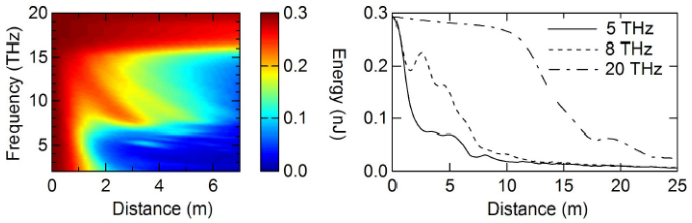

Fig. 3 Energy over 1 THz bandwidth at the pump wavelength as a function of propagation distance. *Left*: false color representation for modulation frequencies over the range 1–20 THz up to a propagation distance of 7 m. *Right*: pump energy over 25 m propagation for selected modulation frequencies as shown

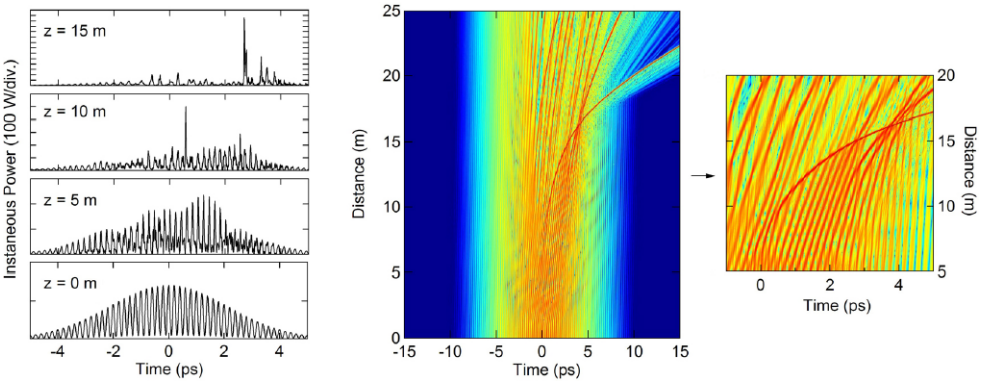

Fig. 4 Dynamics for the spectral broadening in Fig. 1(b) with modulation frequency of 5 THz and amplitude $a_0 = 0.6$. *Left*: line plots of temporal intensity profile at selected distances. *Right*: false color plot of the intensity profile evolution, with a detailed view showing how the largest soliton component collides with and extracts energy from other soliton pulses on the pulse envelope

on the envelope, before clearly separating from the residual envelope in the time domain due to its significantly different group velocity. As mentioned in the introduction, the exchange of energy between colliding solitons in the presence of the Raman effect has been the subject of much previous research [11, 22, 42], and it is likely that this process plays a key role in the statistical excitation of rare rogue wave events in the case where supercontinuum generation arises from noise [14, 15]. The significance of the results shown in Fig. 4 is that they suggest that the study of the propagation dynamics of an initially modulated input may allow this energy exchange process to be studied under controlled (rather than statistical) conditions.

As a final point of discussion, we note that similar qualitative features are observed over a wider range of modulation depths, and Fig. 5 shows false color density plots showing the modulation frequency dependence of the mean output spectra and associated coherence for different values of the modulation depth. Although the detailed interpretation of the results must be carried out on a case-by-case basis, we can clearly see that increased modulation depths are associated with improved coherence in the 0–8 THz range where coherent MI gain processes are significant. This can be readily understood from the fact that the strong conversion regime where coherently seeded MI initiates the SC process is only reached for larger values of the modulation depths, in which case the influence of spontaneous MI is strongly reduced, and overall coherence is enhanced.

4 Conclusions

In this work we have investigated the possibility of controlling the generation of supercontinuum in the long-pulse regime through modulation of the input pulse. Our results indicate that, depending on the value of the modulation frequency and depth, the mean supercontinuum spectral shape can be significantly modified. In addition, we have shown

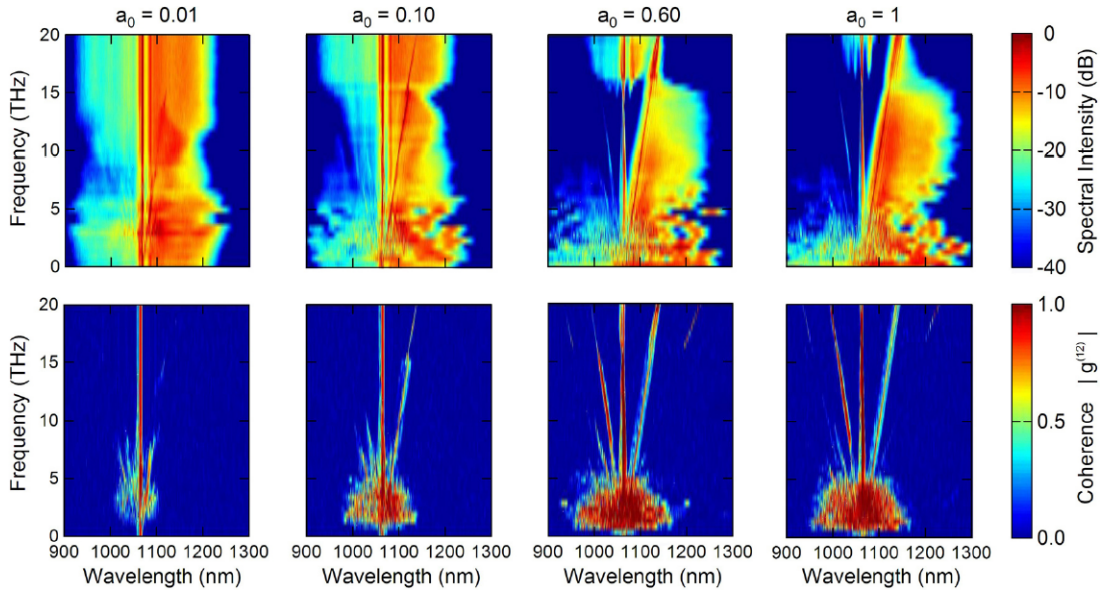

Fig. 5 *Top*: false color density plots of output spectra as functions of modulation frequency for four values of modulation index as indicated. *Bottom*: corresponding plots of the mutual coherence function

that, for large values of the modulation depth and modulation frequencies in a range determined by the initial MI-Raman gain, SC spectra with extended bandwidth and improved stability can be generated. These results may find application in the tailoring of broadband SC spectra for specific applications.

Acknowledgements We thank the *Institut Universitaire de France*, the *Agence Nationale de Recherche* (ANR, Projet SOFICARS), and the Academy of Finland (Grant 121953) for support. We also acknowledge valuable discussions with members of the French national GDR research network PHONOMI2 and the European COST299 Action.

References

1. J.K. Ranka, R.S. Windeler, A.J. Stentz, Visible continuum generation in air-silica microstructure optical fibers with anomalous dispersion at 800 nm. Opt. Lett. **25**, 25–27 (2000)
2. A.V. Husakou, J. Herrmann, Supercontinuum generation of higher-order solitons by fission in photonic crystal fibers. Phys. Rev. Lett. **87**(1–4), 203901 (2001)
3. A.L. Gaeta, Nonlinear propagation and continuum generation in microstructured optical fibers. Opt. Lett. **27**, 924–926 (2002)
4. K.L. Corwin, N.R. Newbury, J.M. Dudley, S. Coen, S.A. Diddams, K. Weber, R.S. Windeler, Fundamental noise limitations to supercontinuum generation in microstructure fiber. Phys. Rev. Lett. **90**(1–4), 113904 (2003)
5. J.M. Dudley, G. Genty, S. Coen, Supercontinuum generation in photonic crystal fiber. Rev. Mod. Phys. **78**, 1135–1184 (2006)
6. M.N. Islam, G. Sucha, I. Bar-Joseph, M. Wegener, J.P. Gordon, D.S. Chemla, Broad bandwidths from frequency-shifting solitons in fibers. Opt. Lett. **14**, 370–372 (1989)
7. M.N. Islam, G. Sucha, I. Bar-Joseph, M. Wegener, J.P. Gordon, D.S. Chemla, Femtosecond distributed soliton spectrum in fibers. J. Opt. Soc. Am. B **6**, 1149–1158 (1989)
8. F. Vanholsbeeck, S. Martín-López, M. González-Herráez, S. Coen, The role of pump incoherence in continuous-wave supercontinuum generation. Opt. Express **13**, 6615–6625 (2005)
9. S.M. Kobtsev, S.V. Kukarin, N.V. Fateev, S.V. Smirnov, Coherent, polarization and temporal properties of self-frequency shifted solitons generated in polarization-maintaining microstructured fibre. Appl. Phys. B **81**, 265–269 (2005)
10. J.N. Kutz, C. Lyngå, B.J. Eggleton, Enhanced supercontinuum generation through dispersion-management. Opt. Express **13**, 3989–3998 (2005)
11. M.H. Frosz, O. Bang, A. Bjarklev, Soliton collision and Raman gain regimes in continuous-wave pumped supercontinuum generation. Opt. Express **14**, 9391–9407 (2006). http://www.opticsexpress.org/abstract.cfm?URI=oe-14-20-9391
12. A. Demircan, U. Bandelow, Analysis of the interplay between soliton fission and modulation instability in supercontinuum generation. Appl. Phys. B **86**, 31–39 (2007)
13. B.A. Cumberland, J.C. Travers, S.V. Popov, J.R. Taylor, 29 W High power CW supercontinuum source. Opt. Express **16**, 5954–5962 (2008). http://www.opticsexpress.org/abstract.cfm?URI=oe-16-8-5954
14. D.R. Solli, C. Ropers, P. Koonath, B. Jalali, Optical rogue waves. Nature **450**, 1054–1058 (2007)
15. J.M. Dudley, G. Genty, B.J. Eggleton, Harnessing and control of optical rogue waves in supercontinuum generation. Opt. Express **16**, 3644–3651 (2008). http://www.opticsexpress.org/abstract.cfm?URI=oe-16-6-3644
16. C.R. Menyuk, Non-Gaussian corrections to the Gordon–Haus distribution resulting from soliton interactions. Opt. Lett. **20**, 285–287 (1995)
17. F.K. Abdullaev, S.A. Darmanyan, F. Lederer, Evolution of randomly modulated solitons in optical fibers. Opt. Commun. **126**, 89–94 (1996)
18. T. Georges, Study of the non-Gaussian timing jitter statistics induced by soliton interaction and filtering. Opt. Commun. **123**, 617–623 (1996)
19. G.E. Falkovich, M.G. Stepanov, S.K. Turitsyn, Statistics of interacting optical solitons. Phys. Rev. E **64**, 067602 (2001)

20. S.A. Derevyanko, S.K. Turitsyn, D.A. Yakushev, Non-Gaussian statistics of an optical soliton in the presence of amplified spontaneous emission. Opt. Lett. **28**, 2097–2099 (2003)
21. Y.J. Chung, A. Peleg, Strongly non-Gaussian statistics of optical soliton parameters due to collisions in the presence of delayed Raman response. Nonlinearity **18**, 1555–1574 (2005)
22. A. Peleg, Intermittent dynamics, strong correlations, and bit-error-rate in multichannel optical fiber communication systems. Phys. Lett. A **360**, 533–538 (2007)
23. A. Peleg, Raman cross talk between optical solitons as a random cascade model. arxiv:0706.4333v1 (2007)
24. N. Korneev, E.A. Kuzin, B. Ibarra-Escamilla, M. Bello-Jimènez, A. Flores-Rosas, Initial development of supercontinuum in fibers with anomalous dispersion pumped by nanosecond-long pulses. Opt. Express **16**, 2636–2645 (2008). http://www.opticsexpress.org/abstract.cfm?URI=oe-16-4-2636
25. S.M. Kobtsev, S.V. Kukarin, S.V. Smirnov, N.V. Fateev, Control of the spectral and coherent properties of a supercontinuum with pronounced soliton structures in the spectrum by using phase-modulated femtosecond pump pulses. Quantum Electron. **37**, 1038–1042 (2007)
26. D. Türke, J. Teipel, H. Giessen, Manipulation of supercontinuum generation by stimulated cascaded four-wave mixing in tapered fibres. Appl. Phys. B **92**, 159 163 (2008)
27. A. Efimov, A.J. Taylor, Supercontinuum generation and soliton timing jitter in SF6 soft glass photonic crystal fibers. Opt. Express **16**, 5942–5953 (2008). http://www.opticsexpress.org/abstract.cfm?URI=oe-16-8-5942
28. T.J. Ellingham, J.D. Ania-Castañón, S.K. Turitsyn, A.A. Pustovskikh, S.M. Kobtsev, M.P. Fedoruk, Dual-pump Raman amplification with increased flatness using modulation instability. Opt. Express **13**, 1079–1084 (2005)
29. S.V. Smirnov, J.D. Ania-Castañón, T.J. Ellingham, S.M. Kobtsev, S.V. Kukarin, S.K. Turitsyn, Optical spectral broadening and supercontinuum generation in telecom applications. Opt. Fiber. Technol. **12**, 122–147 (2006)
30. S.M. Kobtsev, S.V. Smirnov, Influence of noise amplification on generation of regular short pulse trains in optical fibre pumped by intensity-modulated CW radiation. Opt. Express **16**, 7428–7434 (2008). http://www.opticsexpress.org/abstract.cfm?URI=oe-16-10-7428
31. D.R. Solli, C. Ropers, B. Jalali, Demonstration of stimulated supercontinuum generation—an optical tipping point. arXiv:0801.4066v1 [physics.optics] (2008)
32. K.J. Blow, D. Wood, Theoretical description of transient stimulated Raman scattering in optical fibers. IEEE J. Quantum Electron. **25**, 2665–2673 (1989)
33. R.H. Stolen, J.P. Gordon, W.J. Tomlinson, H.A. Haus, Raman response function of silica-core fibers. J. Opt. Soc. Am. B **6**, 1159–1166 (1989)
34. G.P. Agrawal, *Nonlinear Fiber Optics*, 4th edn. (Academic Press, San Diego, 2006)
35. P.D. Drummond, J.F. Corney, Quantum noise in optical fibers. I. Stochastic equations. J. Opt. Soc. Am. B **18**, 139–152 (2001)
36. E.J. Greer, D.M. Patrick, P.G.J. Wigley, J.R. Taylor, Generation of 2 THz repetition rate pulse trains through induced modulational instability. Electron. Lett. **25**, 1246–1248 (1989)
37. P.V. Mamyshev, S.V. Chernikov, E.M. Dianov, Generation of fundamental soliton trains for high-bit-rate optical fiber communication lines. IEEE J. Quantum Electron. **27**, 2347–2355 (1991)
38. J.M. Dudley, F. Gutty, S. Pitois, G. Millot, Complete characterization of terahertz pulse trains generated from nonlinear processes in optical fibers. IEEE J. Quantum Electron. **37**, 587–594 (2001)
39. J.M. Dudley, S. Coen, Coherence properties of supercontinuum spectra generated in photonic crystal and tapered optical fibers. Opt. Lett. **27**, 1180–1182 (2002)
40. F. Vanholsbeeck, Ph. Emplit, S. Coen, Complete experimental characterization of the influence of parametric four-wave mixing on stimulated Raman gain. Opt. Lett. **28**, 1960–1962 (2003)
41. G. Cappellini, S. Trillo, Third-order three-wave mixing in single-mode fibers: exact solutions and spatial instability effects. J. Opt. Soc. Am. B **8**, 824–838 (1991)
42. F. Luan, D.V. Skryabin, A.V. Yulin, J.C. Knight, Energy exchange between colliding solitons in photonic crystal fibers. Opt. Express **14**, 9844–9853 (2006). http://www.opticsexpress.org/abstract.cfm?URI=oe-14-21-9844